Direct Interfacing of Average-Value Models of VSCs in PSCAD/EMTDC

Seyyedmilad Ebrahimi
Department of Electrical and Computer Engineering
The University of British Columbia
Vancouver, Canada
ebrahimi@ece.ubc.ca

Taleb Vahabzadeh
Department of Electrical and Computer Engineering
The University of British Columbia
Vancouver, Canada
talebv@ece.ubc.ca

Juri Jatskevich
Department of Electrical and Computer Engineering
The University of British Columbia
Vancouver, Canada
jurij@ece.ubc.ca

***Abstract*—Voltage-source converters (VSCs) are widely utilized in power systems. Due to their high-frequency switching, discrete detailed models of VSCs are computationally expensive in system-level simulations, and their average-value models (AVMs) have proven indispensable for fast/efficient studies. Conventional AVMs of VSCs use dependent current/voltage sources to interface with external circuits. In PSCAD/EMTDC, with a non-iterative solution, the interfacing variables are computed based on the values of the input voltages/currents from the previous time-step. This one-time-step delay can make the results numerically inaccurate/unstable when large time-steps are used in simulations. In this paper, an AVM is developed for VSCs that is directly interfaced with external circuits without delays to allow large time-step. This is done by formulating the equivalent conductance matrix of the VSC AVM which is merged into (and solved simultaneously with) the rest of the network nodal equations. The new directly-interfaced AVM of VSCs is verified in PSCAD/EMTDC against the classic dependent-source-based AVM and is demonstrated to outperform the existing approach in terms of numerical accuracy at large time-steps.**

***Index Terms*-- Average-value model, conductance matrix, interfacing, nodal, numerical, simulation, VSC.**

I. INTRODUCTION

VOLTAGE-SOURCE converters (VSCs) possess various advantageous properties, including (but not limited to) independent control of active and reactive power [1], low harmonic distortions, etc. As a result, VSCs are dominantly utilized in many applications, e.g., wind energy conversion systems, FACTS devices, HVDC light systems [2], modern vehicular, marine, aircraft power systems, etc.

Design, study, and analysis of such systems rely on many electromagnetic transient (EMT) simulations [3] that are conducted either offline and/or in real-time, e.g., for stability analysis [4], dynamic design/tune of controllers, etc. In such studies, it is desirable to use as much large as possible time-steps for simulations in order to conduct the studies in a shorter amount of time and/or to be able to simulate larger networks on a given computational hardware [5], [6].

The VSCs typically operate with high-frequency switching in the order of several kilo-Hertz. The detailed switching models of VSCs reconstruct the discrete waveforms very accurately; however, they require accordingly small time-steps and/or interpolations [7], [8], for predicting the exact discrete switching events. This renders a heavy computational burden on the simulators and poses a limit on the size of the system.

To address this issue, average-value models (AVMs) have been developed for VSCs where the discrete switching details are neglected and slower average dynamics are captured [9]. Since the AVMs are independent of the switching events, they can be simulated with much larger time-steps and are computationally more efficient compared to the switching models. Conventionally, the AVMs of VSCs are implemented using dependent current/voltage sources at the interface with external networks. In PSCAD/EMTDC, with a non-iterative solution, a one-time-step relaxation delay is needed to compute the interfacing variables (based on the values of the computed inputs from the previous time-step). This delay in the so-called indirect interfacing may lead to numerically inaccurate/ unstable solutions at large time-steps, which defies the benefits of using the AVMs for VSCs. The control feedback loops in VSC-based systems may also necessitate the use of a time-step relaxation delay in non-iterative solutions [10].

Recently, a direct interfacing technique was developed for AVMs of power-electronic converters in nodal-analysis-based solutions [11], [12] that eliminates the artificial interfacing time-step delay inherent to the classic dependent-source-based AVMs. Inspired by [11], [12], in this paper, a new AVM for VSCs is developed with direct interfacing with external circuits in PSCAD/EMTDC program with a non-iterative solution. This is achieved by formulating the VSC AVM relations in the general nodal form and obtaining a distinct conductance matrix for the VSC. This allows to combine/merge the AVM as a sub-matrix into the conductance matrix of the rest of the network, as opposed to using dependent/controlled sources for the interface. As a result, the AVM relations are simultaneously solved as part of the overall network with the external system. This avoids the relaxation time-step delay and allows using large time-step sizes for simulation.

The numerical accuracy of the new directly-interfaced AVM is investigated in a VSC-based energy conversion system where the effect of voltage/power/current control loops is also considered. It is demonstrated that the new AVM outperforms the existing classic AVMs of VSCs and can be simulated with very large time steps. This can represent a valuable advancement and asset for offline and/or real-time simulation of VSC-based systems where large time-steps are desirable.

2022 IEEE Electrical Power and Energy Conference (EPEC) | 978-1-6654-6318-8/22/$31.00 ©2022 IEEE | DOI: 10.1109/EPEC56903.2022.9999746

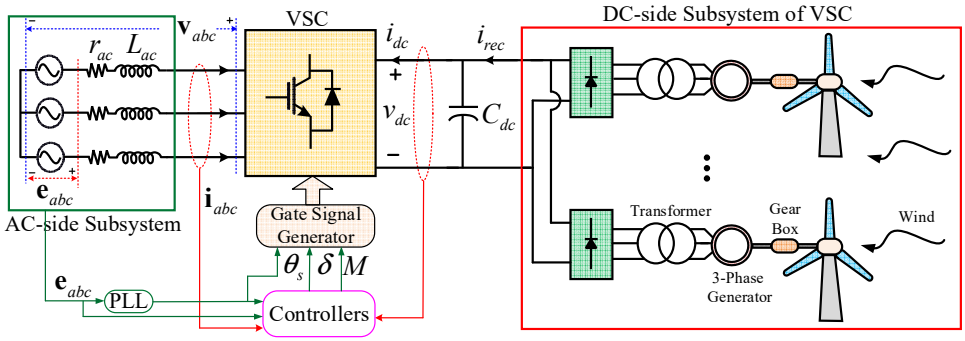

Fig. 1. A generic VSC-based wind power generation system.

II. VSC-Based AC–DC System

In this paper, it is assumed that a voltage-source converter is utilized as the interface between ac-side and dc-side subsystems in a wind power generation system, as shown in Fig. 1. Therein, the ac-side subsystem may be an electric grid which is represented by its Thévenin equivalent circuit composed of the three-phase voltages $\mathbf{e}_{abc}$ and the series impedances r_{ac} and L_{ac} (which may also represent the series filter of the converter). The dc-side terminals of the VSC are connected to a dc-link capacitor C_{dc} and a dc-side subsystem, which may be composed of ac–dc rectifiers (e.g., six-pulse diode bridges) fed by a cluster of three-phase generators (e.g., permanent magnet synchronous generator, induction generator, doubly-fed induction generator, etc.) driven by wind turbines.

As shown in Fig. 1, the ac- and dc-side variables of the VSC are captured and used in the controller block which establishes the input variables for the VSC gate signal generator block. The controllers comprise outer active/reactive power (and/or voltage-level) control loops in addition to inner current control loops which are typically implemented in the *qd* coordinates [13]. The schematic of the controllers is shown in Fig. 2, where (without loss of generality) the dc voltage and reactive power control loops are adopted.

The *abc*/*qd* transformations in the controller block as well as the gate signal generator require the angle of the fundamental frequency components of the Thévenin equivalent voltages denoted by $\mathbf{e}_{abc}$ and their angle θ_s, with respect to which the VSC output ac voltages are established. The angle θ_s is typically obtained using a phase-locked-loop (PLL). The *abc*/*qd* transformations are performed as

$$\mathbf{e}_{qd} = \begin{bmatrix} e_q \\ e_d \end{bmatrix} = [\mathbf{K}(\theta_s)]\mathbf{e}_{abc}, \tag{1}$$

$$\mathbf{i}_{qd} = \begin{bmatrix} i_q \\ i_d \end{bmatrix} = [\mathbf{K}(\theta_s)]\mathbf{i}_{abc}, \tag{2}$$

using Park's transformation matrix $\mathbf{K}(\theta_s)$ defined as [14]

$$\mathbf{K}(\theta_s) = \frac{2}{3}\begin{bmatrix} \cos(\theta_s) & \cos(\theta_s - 2\pi/3) & \cos(\theta_s + 2\pi/3) \\ \sin(\theta_s) & \sin(\theta_s - 2\pi/3) & \sin(\theta_s + 2\pi/3) \end{bmatrix}. \tag{3}$$

The transformations are also graphically illustrated with vector diagrams in Fig. 3. As seen in Fig. 3, the *q*-axis of the *qd* frame is assumed to be aligned with the phase *a* source

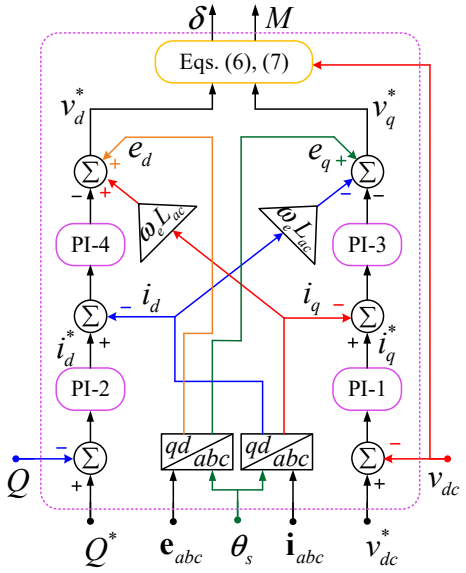

Fig. 2. Schematic of the outer voltage/power and inner current control loops for the voltage-source converter using four PI controllers.

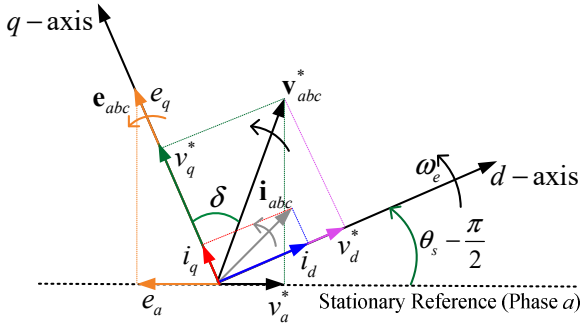

Fig. 3. Vector diagram of the three-phase ac voltages and currents in stationary and rotating *qd* reference frames.

voltage e_a (at time zero) which results in having $e_d = 0$. As seen in the control diagram in Fig. 2, the transformed *qd* variables $\mathbf{e}_{qd}$ and $\mathbf{i}_{qd}$ are used along with the captured currents/voltages as well as the set-points for the dc voltage (v_{dc}^*) and reactive power (Q^*) to compute the set-points for the *qd* voltages (i.e., v_q^* and v_d^*) through the four PI controllers. The VSC constructs the required $\mathbf{v}_{qd}^*$ voltages with high-frequency switching operation. The fundamental frequency components of the VSC output ac voltages can be expressed as

$$\mathbf{v}^1_{abc} = \begin{bmatrix} v^1_a \\ v^1_b \\ v^1_c \end{bmatrix} = A \begin{bmatrix} \cos(\theta_s - \delta) \\ \cos(\theta_s - \delta - 2\pi/3) \\ \cos(\theta_s - \delta + 2\pi/3) \end{bmatrix}, \quad (4)$$

where

$$A = \sqrt{\left(v^*_q\right)^2 + \left(v^*_d\right)^2}, \quad (5)$$

and

$$\delta = \tan^{-1}\left(v^*_d / v^*_q\right). \quad (6)$$

Here, δ is the phase shift between the fundamental frequency components of the VSC output voltages and the fundamental frequency components of the Thévenin equivalent sources.

In addition to the angles θ_s and δ, the VSC gate signal generator requires the so-called modulation index M which specifies the amplitude of the VSC ac output voltages with respect to its dc terminal voltage. Various switching strategies require different modulation indices [9]. Here, it is assumed that sinusoidal-pulse-width-modulation (SPWM) is adopted for which the modulation index is defined as

$$M = \frac{A}{(1/2)v_{dc}} = \frac{\sqrt{\left(v^*_q\right)^2 + \left(v^*_d\right)^2}}{(1/2)v_{dc}}. \quad (7)$$

It is worth mentioning that the methodology presented in this paper is applicable to other switching methods [14] with different definitions of M and the formulations can be readily updated/modified accordingly.

III. Average-Value Models of VSCs

In the average-value models (AVMs), the switching ripples are neglected and the relations of the terminal variables of the VSC are established between the fast average values of the dc-side waveforms and the fundamental frequency components of the ac-side *abc* variables (or average values of transformed *qd* variables). The fast averaging is defined over a switching period T_{sw} as

$$\bar{x}(t) = \frac{1}{T_{sw}} \int_{t-T_{sw}}^{t} x(t)d\tau, \qquad T_{sw} = \frac{1}{f_{sw}}, \quad (8)$$

where f_{sw} is the switching frequency of the VSC; the variable x denoting the dc or transformed *qd* currents and/or voltages, with $\bar{x}$ denoting their average value.

For the purpose of establishing the AVMs, it is assumed that the (fundamental frequency components of the) ac currents are transformed to the *qd* coordinates similar to (2) as

$$\bar{\mathbf{i}}_{qd} = \begin{bmatrix} \bar{i}_q \\ \bar{i}_d \end{bmatrix} = [\mathbf{K}(\theta_s)] \begin{bmatrix} i^1_a & i^1_b & i^1_c \end{bmatrix}^T, \quad (9)$$

which results in averaged $\bar{\mathbf{i}}_{qd}$ currents. Afterward, the averaged *qd* variables (i.e., $\bar{\mathbf{i}}_{qd}$ and then computed $\bar{\mathbf{v}}_{qd}$) which correspond to the fundamental frequency components of the *abc* variables (i.e., $\mathbf{i}^1_{abc}$ and $\mathbf{v}^1_{abc}$) are related to the average values of the dc-side variables (i.e., $\bar{i}_{dc}$ and $\bar{v}_{dc}$).

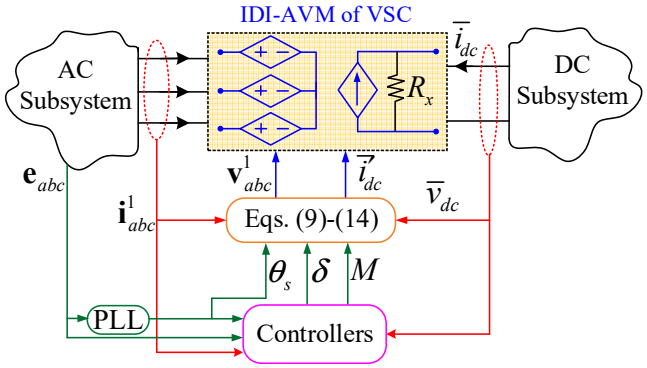

Fig. 4. Implementation of the conventional IDI-AVM of VSCs and its circuit interface with external subsystems using dependent current/voltage sources.

A. Conventional Indirectly-Interfaced AVM

In the conventional indirectly-interfaced AVMs (IDI-AVMs) of VSCs [9], the semiconductor switches are replaced with dependent current/voltage sources, as demonstrated in Fig. 4. A snubber resistor R_x may be needed in parallel with the dc-side current source for numerical damping depending on the composition of the dc subsystem. Assuming a lossless converter and using the input/output power balance, the controlled dc current source can be computed as [9]

$$\vec{i}_{dc} = \frac{3}{4} M \cos(\varphi) \left\| \bar{\mathbf{i}}_{qd} \right\|, \quad (10)$$

where φ is the so-called displacement angle of the VSC and is obtained as

$$\varphi = \tan^{-1}\left(\bar{i}_d / \bar{i}_q\right) - \delta. \quad (11)$$

The averaged $\bar{\mathbf{v}}_{qd}$ voltages can also be expressed based on (6), (7) as

$$\bar{\mathbf{v}}_{qd} = \begin{bmatrix} \bar{v}_q \\ \bar{v}_d \end{bmatrix} = \frac{1}{2} M \begin{bmatrix} \cos(\delta) \\ \sin(\delta) \end{bmatrix} \bar{v}_{dc}. \quad (12)$$

Therefore, the controlled ac voltage sources $\mathbf{v}^1_{abc}$ at the interface in Fig. 4 can be obtained by transforming the $\bar{\mathbf{v}}_{qd}$ voltages in (12) to the *abc* coordinates as

$$\mathbf{v}^1_{abc} = \begin{bmatrix} v^1_a & v^1_b & v^1_c \end{bmatrix}^T = [\mathbf{K}(\theta_s)]^{-1} \bar{\mathbf{v}}_{qd}, \quad (13)$$

where $[\mathbf{K}(\theta_s)]^{-1}$ is the inverse of Park's transformation matrix defined as [14]

$$[\mathbf{K}(\theta_s)]^{-1} = \begin{bmatrix} \cos(\theta_s) & \sin(\theta_s) \\ \cos(\theta_s - 2\pi/3) & \sin(\theta_s - 2\pi/3) \\ \cos(\theta_s + 2\pi/3) & \sin(\theta_s + 2\pi/3) \end{bmatrix}. \quad (14)$$

In PSCAD/EMTDC program, the ac currents $\mathbf{i}^1_{abc}$ and the dc voltage $\bar{v}_{dc}$ [that are used in (9)–(14) for calculation of the interfacing variables $\mathbf{v}^1_{abc}$ and $\vec{i}_{dc}$ in Fig. 4] need to be computed by the ac and dc subsystems. Therefore, their solution will only become available for the next time-step. As a result, the program needs to use the values of the inputs $\mathbf{i}^1_{abc}$ and $\bar{v}_{dc}$ calculated at the previous time-step [i.e., $\bar{v}_{dc}(t - \Delta t)$ and $\mathbf{i}^1_{abc}(t - \Delta t)$] for calculating $\mathbf{v}^1_{abc}(t)$ and $\vec{i}_{dc}(t)$ as

$$\begin{bmatrix} v_a^1(t) & v_b^1(t) & v_c^1(t) \end{bmatrix}^T = \left[\mathbf{K}(\theta_s)\right]^{-1} \frac{1}{2} M \begin{bmatrix} \cos(\delta) \\ \sin(\delta) \end{bmatrix} \bar{v}_{dc}(t-\Delta t), \quad (15)$$

$$\bar{i}'_{dc}(t) = \frac{3}{4} M \cos\left(\tan^{-1}\left(\bar{i}_d / \bar{i}_q\right) - \delta\right) \left\| \bar{\mathbf{i}}_{qd} \right\|, \quad \begin{bmatrix} \bar{i}_q \\ \bar{i}_d \end{bmatrix} = \left[\mathbf{K}(\theta_s)\right] \begin{bmatrix} i_a^1(t-\Delta t) \\ i_b^1(t-\Delta t) \\ i_c^1(t-\Delta t) \end{bmatrix}. \quad (16)$$

This one time-step Δt delay for the dependent sources at the interface is inherent/inevitable in the IDI-AVMs, which may lead to numerical errors and/or instability in the solutions when the time-step size Δt is large [11].

B. Proposed Directly-Interfaced AVM

In the directly-interfaced AVM (DI-AVM) of VSCs, the relations of the terminal variables of the VSC are established in the general nodal form as

$$\mathbf{G}_{\text{VSC}}(t) \cdot \mathbf{v}_{\text{VSC}}(t) = \mathbf{i}_{\text{VSC}}(t), \quad (17)$$

where

$$\mathbf{v}_{\text{VSC}}(t) = \begin{bmatrix} v_a^1(t) \\ v_b^1(t) \\ v_c^1(t) \\ \bar{v}_{dc}(t) \end{bmatrix}, \quad \mathbf{i}_{\text{VSC}}(t) = \begin{bmatrix} i_a^1(t) \\ i_b^1(t) \\ i_c^1(t) \\ \bar{i}_{dc}(t) \end{bmatrix}, \quad (18)$$

and $\mathbf{G}_{\text{VSC}}(t)$ is the conductance matrix of the converter.

Having a separate sub-matrix for the VSC conductance allows merging it into the overall system conductance matrix. Consequently, the nodal equations of the VSC would be solved simultaneously as part of the overall network nodal equations; and the one Δt interfacing delay existing in the IDI-AVMs would be eliminated, allowing to use large time-steps for simulations.

To obtain the VSC formulation in the form of (17), the dc-side voltage is expressed based on (10) and Fig. 4 as

$$\bar{v}_{dc}(t) = R_x\left(\bar{i}'_{dc}(t) + \bar{i}_{dc}(t)\right) = R_x\left(\frac{3}{4} M \sqrt{\left(\bar{i}_q(t)\right)^2 + \left(\bar{i}_d(t)\right)^2} \cos(\varphi) + \bar{i}_{dc}(t)\right). \quad (19)$$

The ac-side transformed *qd* voltages can also be expressed based on (12), (19) as

$$\begin{cases} \bar{v}_q(t) = \frac{1}{2} M R_x \cos(\delta)\left(\frac{3}{4} M \sqrt{\left(\bar{i}_q(t)\right)^2 + \left(\bar{i}_d(t)\right)^2} \cos(\varphi) + \bar{i}_{dc}(t)\right) \\ \bar{v}_d(t) = \frac{1}{2} M R_x \sin(\delta)\left(\frac{3}{4} M \sqrt{\left(\bar{i}_q(t)\right)^2 + \left(\bar{i}_d(t)\right)^2} \cos(\varphi) + \bar{i}_{dc}(t)\right) \end{cases}. \quad (20)$$

In (19), (20), the term $\cos(\varphi)$ can be written based on (11) and after trigonometric manipulations as

$$\cos(\varphi) = \cos\left(\tan^{-1}\left(\bar{i}_d(t)/\bar{i}_q(t)\right) - \delta\right) = \frac{\bar{i}_q(t)}{\sqrt{\left(\bar{i}_q(t)\right)^2 + \left(\bar{i}_d(t)\right)^2}} \cos(\delta) + \frac{\bar{i}_d(t)}{\sqrt{\left(\bar{i}_q(t)\right)^2 + \left(\bar{i}_d(t)\right)^2}} \sin(\delta). \quad (21)$$

Therefore, (19), (20) can be simplified using (21) and re-written in the following form as

$$\begin{bmatrix} \bar{v}_q(t) \\ \bar{v}_d(t) \\ \bar{v}_{dc}(t) \end{bmatrix} = \mathbf{Z}'_{\text{VSC}} \begin{bmatrix} \bar{i}_q(t) \\ \bar{i}_d(t) \\ \bar{i}_{dc}(t) \end{bmatrix}, \quad (22)$$

where $\mathbf{Z}'_{\text{VSC}}$ is defined in (23).

Afterwards, the voltages $\bar{\mathbf{v}}_{qd}(t)$ and the currents $\bar{\mathbf{i}}_{qd}(t)$ in (22) are transformed to the *abc* coordinates similar to (13). This results in the following form of relations for the VSC terminal variables

$$\mathbf{v}_{\text{VSC}}(t) = \mathbf{Z}_{\text{VSC}}(t) \cdot \mathbf{i}_{\text{VSC}}(t), \quad (24)$$

where $\mathbf{Z}_{\text{VSC}}(t)$ is the VSC impedance matrix defined as

$$\mathbf{Z}_{\text{VSC}}(t) = \left[\begin{array}{c|c} \mathbf{Z}_4(t) & \mathbf{Z}_5(t) \\ \hline \mathbf{Z}_5^T(t) & Z_3 \end{array}\right]. \quad (25)$$

The sub-matrices in (25) are expressed in (26), (27)

$$\mathbf{Z}_5(t) = \left[\mathbf{K}(\theta_s)\right]^{-1} \mathbf{Z}_2 = \frac{1}{2} M R_x \begin{bmatrix} \cos(\theta_s - \delta) \\ \cos(\theta_s - \delta - 2\pi/3) \\ \cos(\theta_s - \delta + 2\pi/3) \end{bmatrix}, \quad (27)$$

and $Z_3 = R_x$ as shown in (23).

Finally, the conductance matrix of the VSC, i.e., $\mathbf{G}_{\text{VSC}}(t)$ used in (17) can be computed based on (25)–(27) as

$$\mathbf{G}_{\text{VSC}}(t) = \left[\mathbf{Z}_{\text{VSC}}(t)\right]^{-1}. \quad (28)$$

Having $\mathbf{G}_{\text{VSC}}(t)$ calculated in (28), the DI-AVM of VSCs can be readily implemented using a conductance matrix and interfaced with the external subsystems as demonstrated in Fig. 5. Therein, the $\mathbf{G}_{\text{VSC}}(t)$ matrix is calculated directly using the inputs θ_s, δ, and M based on (25)–(28) without the need for any input from $\mathbf{i}_{abc}^1$ and $\bar{v}_{dc}$ as opposed to Fig. 4 for IDI-AVM.

$$\mathbf{Z}'_{\text{VSC}} = \left[\begin{array}{c|c} \mathbf{Z}_1 & \mathbf{Z}_2 \\ \hline \mathbf{Z}_2^T & Z_3 \end{array}\right] = \left[\begin{array}{cc|c} \frac{3}{8} M^2 R_x \cos^2(\delta) & \frac{3}{16} M^2 R_x \sin(2\delta) & \frac{1}{2} M R_x \cos(\delta) \\ \frac{3}{16} M^2 R_x \sin(2\delta) & \frac{3}{8} M^2 R_x \sin^2(\delta) & \frac{1}{2} M R_x \sin(\delta) \\ \hline \frac{3}{4} M R_x \cos(\delta) & \frac{3}{4} M R_x \sin(\delta) & R_x \end{array}\right]. \quad (23)$$

$$\mathbf{Z}_4(t) = \left[\mathbf{K}(\theta_s)\right]^{-1} \mathbf{Z}_1 \left[\mathbf{K}(\theta_s)\right] = \frac{1}{8} M^2 R_x \begin{bmatrix} 3/2 + \cos(2\theta_s - 2\delta) & \cos(2\theta_s - 2\delta - 2\pi/3) & \cos(2\theta_s - 2\delta + 2\pi/3) \\ \cos(2\theta_s - 2\delta - 2\pi/3) & 3/2 + \cos(2\theta_s - 2\delta + 2\pi/3) & \cos(2\theta_s - 2\delta) \\ \cos(2\theta_s - 2\delta + 2\pi/3) & \cos(2\theta_s - 2\delta) & 3/2 + \cos(2\theta_s - 2\delta - 2\pi/3) \end{bmatrix}. \quad (26)$$

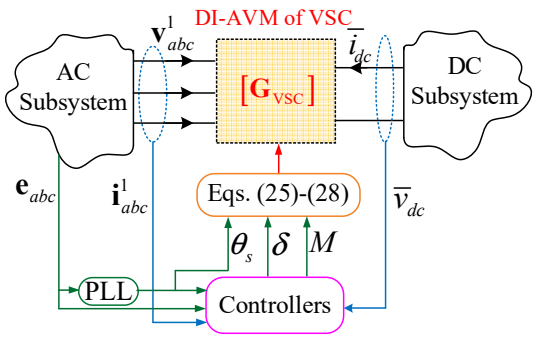

Fig. 5. Implementation of the DI-AVM of VSCs and its circuit interface with external subsystems using a conductance matrix.

IV. Computer Studies

To verify the numerical performance of the proposed DI–AVM of VSCs compared to the classic IDI–AVM, the ac–dc energy conversion system in Fig. 1 has been implemented in PSCAD/EMTDC environment. Three different representations of the VSC are considered in Figs. 6(a)–6(c); i.e., the detailed switching model, the IDI–AVM according to Fig. 4, and the DI–AVM based on Fig. 5. Herein, the DI–AVM in Fig. 6(c) is implemented as a user-defined block whose conductance matrix is added to the conductance matrix of the rest of the system using the EMTDC_ADDGM2 subroutine. The system parameters are summarized in the Appendix. For comparisons, the solution of the classic IDI–AVM obtained with a small time-step of 1 μs is considered as the reference.

For transient studies, without loss of generality, it is assumed that the dc-side subsystem of the VSC in Fig. 1 injects the dc current i_{rec} whose profile undergoes oscillations as shown in Fig. 7(a) due to fluctuations in the wind power. The simulations startup from zero initial conditions while the modulation index M and angle δ for the VSC are set manually to achieve ~200 kV at the dc bus and zero reactive power before the start of the fluctuations at t=2s. Consequently, the VSC voltages/currents undergo fluctuations due/similar to the wind profile of Fig. 7(a) until t=7s. At t=7s, the controllers are activated to regulate the dc-link voltage at 200 kV and the reactive power to zero. The transient response of the system is shown in Figs. 7(b)–(d) for the VSC terminal variables as obtained by the subject models where both IDI–AVM and DI–AVM are executed with a time-step of Δt=10 μs.

As it can be observed in Fig. 7, with such fairly small time-steps, both the IDI– and DI–AVMs obtain accurate results compared to the reference AVM. The results of the AVMs are also consistent with the ones obtained from the detailed switching model (when switching ripples are neglected).

The same transient study shown in Fig. 7 is repeated with a fairly medium-large time-step of Δt=150 μs chosen for IDI–AVM and a very large time-step of Δt=500 μs for the proposed DI–AVM. Some representative dc and ac waveforms from the VSC terminals are depicted in Fig. 8.

As it can be observed in Fig. 8, the IDI–AVM entirely loses its accuracy with Δt=150 μs, while the DI–AVM remains very accurate compared to the reference solution even at Δt=500 μs.

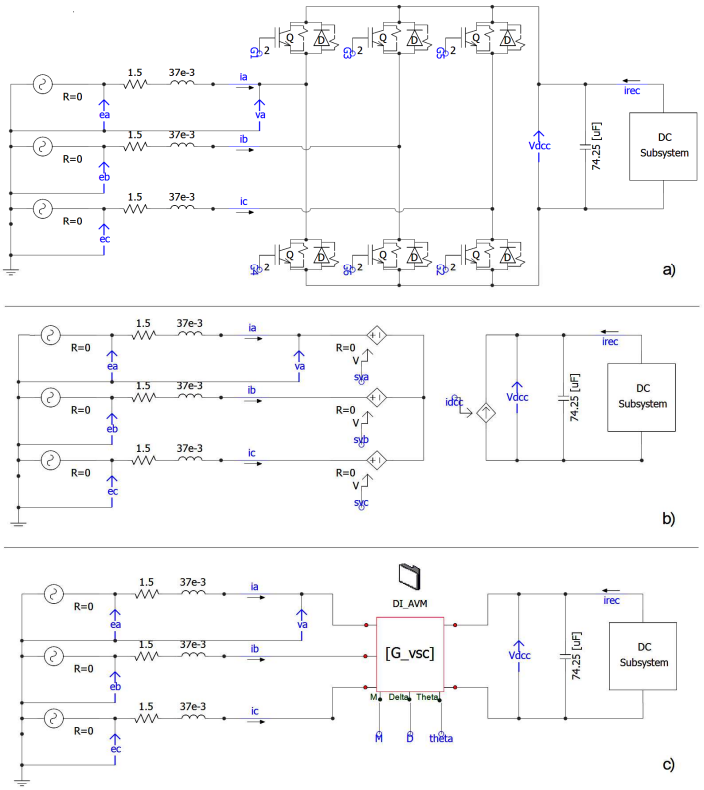

Fig. 6. Implementation and circuit interfacing of the subject models of VSC in PSCAD/EMTDC environment: (a) detailed switching model, (b) IDI-AVM, and (c) proposed DI-AVM.

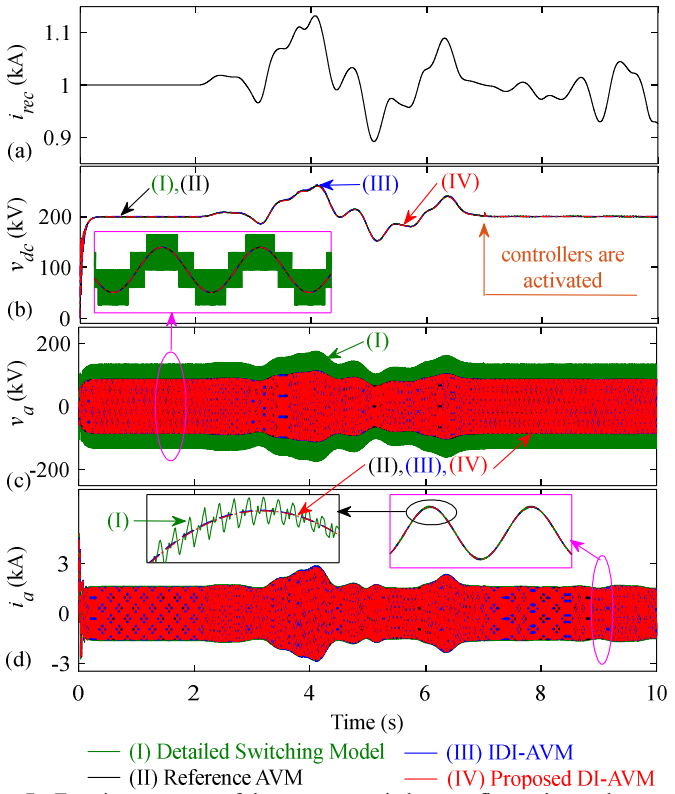

Fig. 7. Transient response of the system to wind power fluctuations, where at t=7 s controllers are activated, as obtained by the subject models for the VSC terminal variables: (a) dc subsystem current, (b) dc-link voltage, (c) VSC phase a voltage, and (d) VSC phase a current.

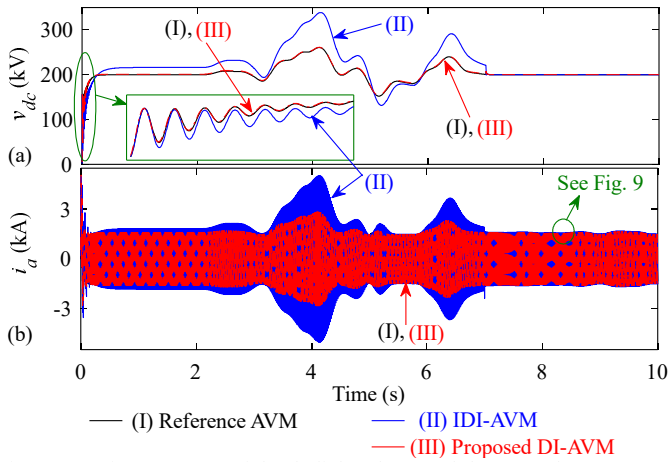

Fig. 8. Transient response of the dc-link voltage and the VSC phase *a* current as obtained by the AVMs with large time-steps: (I) reference AVM with 1 µs, (II) IDI–AVM with 150 µs, and (III) DI–AVM with 500 µs.

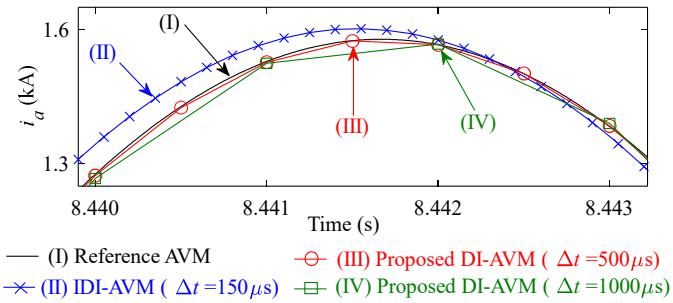

Fig. 9. Magnified view of the ac current in Fig. 8 as obtained by the IDI–AVM and DI–AVM at different time-steps compared to the reference AVM.

It can also be observed in Fig. 8 that the deviations in the IDI–AVM initiate from the startup due to the inaccuracy caused by the one-time-step delay at such a fairly medium-large step size.

It is worthwhile to mention that after the activation of the controllers at t=7s, the error in the IDI–AVM is fairly compensated by the PI controllers and the solution follows the reference more accurately. However, the compensation is less effective for the ac variables, as shown in Fig. 9 for the magnified view of ac current after the controllers are activated. As seen in Fig. 9, the solution of the IDI–AVM has visibly deviated from the reference even with the compensation from the PIs. It is also noted that the compensation phenomenon cannot avoid/mitigate the numerical inaccuracy/instability at larger time-steps. It was verified that for this study and given the system parameters, the IDI–AVM can produce acceptable results only with time-steps not greater than 10~20 µs.

Meanwhile, the proposed DI–AVM provides very accurate results that exactly land on the reference solution even with very large-time steps, as demonstrated in Fig. 9. Therein, the results of the DI–AVM run with Δt=1000 µs are also superimposed which verify the excellent accuracy of the proposed DI–AVM at very large time-steps.

V. Conclusion

In this paper, a new average-value model for voltage-source converters has been developed that is directly interfaced with external circuits as a conductance matrix in PSCAD/EMTDC. As a result, the new directly-interfaced AVM (DI–AVM) avoids the time-step delay inherent to the classic dependent-source-based AVMs; thus, allowing to use large time-steps for simulations. The numerical advantages of the new DI–AVM have been demonstrated and it was verified that the DI–AVM can run with time-steps as large as ~1000 µs while staying accurate. It is envisioned that the newly developed DI–AVM of VSCs can become a beneficial asset for offline and/or real-time simulators when large time-steps are desirable.

Appendix

Parameters of Case-Study System:

$|\mathbf{e}_{abc}|_{phase}^{rms} = 57$ kV , $f_e = 60$ Hz , $r_{ac} = 1.5\ \Omega$, $L_{ac} = 37$ mH , $C_{dc} = 74.25$ µF .

Parameters of PI Controllers:

Outer loops (PI-1, PI-2): $K_p = 0.313$, $\tau_1 = 0.052$ s ,

Inner loops (PI-3, PI-4): $K_p = 10.29$, $\tau_1 = 0.268$ s .

References

[1] W. Wang, A. Beddard, M. Barnes and O. Marjanovic, "Analysis of active power control for VSC–HVDC," *IEEE Trans. Power Del*., vol. 29, no. 4, pp. 1978–1988, Aug. 2014.

[2] S. Li, T. A. Haskew and L. Xu, "Control of HVDC light system using conventional and direct current vector control approaches," *IEEE Trans. Power Electron*., vol. 25, no. 12, pp. 3106–3118, Dec. 2010.

[3] H. W. Dommel, "Digital computer solution of electromagnetic transients in single and multiphase networks," *IEEE Trans. Power App. and Syst.*, vol. PAS-88, no. 4, pp. 388–399, Apr. 1969.

[4] Y. Gu and T. C. Green, "Power system stability with a high penetration of inverter-based resources," *Proc. IEEE,* doi: 10.1109/JPROC.2022.

[5] RTDS Technologies Applications, Superstep. 2022. [Online]. Available: https://knowledge.rtds.com/hc/en-us/articles/360034827413-Superstep.

[6] J. Mahseredjian, V. Dinavahi, and J. A. Martinez, "Simulation tools for electromagnetic transients in power systems: Overview and challenges," *IEEE Trans. Power Del*, vol. 24, no. 3, pp. 1657–1669, Jul. 2009.

[7] M.O. Faruque, V. Dinavahi, and Wilsun Xu, "Algorithms for the accounting of multiple switching events in digital simulation of power-electronic systems," *IEEE Trans. Power Del*., vol. 20, no. 2, pp. 1157–1167, Apr. 2005.

[8] EMTDC User's Guide v4.6, "Chapter 4: Advanced features, Interpolation and switching", 2018. [Online]. Available: https://www.pscad.com/knowledge-base/article/163.

[9] Chiniforoosh *et al*., "Definitions and applications of dynamic average models for analysis of power systems," *IEEE Trans. Power Del*., vol. 25, no. 4, pp. 2655–2669, Oct. 2010.

[10] J. Mahseredjian, L. Dubé, M. Zou, S. Dennetière, and G. Joos, "Simultaneous solution of control system equations in EMTP," *IEEE Trans. Power Syst*, vol. 21, no. 1, pp. 117–124, Feb. 2006.

[11] S. Ebrahimi, H. Atighechi, S. Chiniforoosh, and J. Jatskevich, "Direct interfacing of parametric average-value models of ac–dc converters for nodal analysis-based solution," *IEEE Trans. Energy Convers.*, early access, doi: 10.1109/TEC.2022.3177131.

[12] S. Ebrahimi and J. Jatskevich, "Average-value model for voltage-source converters with direct interfacing in EMTP-type solution," accepted in *IEEE Trans. Energy Convers*.

[13] W. Taha, A. R. Beig and I. Boiko, "Design of PI controllers for a grid-connected VSC based on optimal disturbance rejection," in *Proc. IEEE 41st Ind. Electr. Soc. Annual Conf.* (*IECON*), 2015, pp. 1954–1959.

[14] P. C. Krause, O. Wasynczuk, S. D. Sudhoff, and S. Pekarek, "Analysis of electric machinery and drive systems," 3rd Edition, IEEE Press, Piscataway, NJ, 2013.